

Fragmentation and dynamics of dense gas structures in the proximity of massive young stellar object W42-MME

N. K. Bhadari^{1,2*}, L. K. Dewangan¹, L. E. Pirogov³, A. G. Pazukhin³, I. I. Zinchenko³,
A. K. Maity^{1,2}, and Saurabh Sharma⁴

¹Physical Research Laboratory, Navrangpura, Ahmedabad 380009, India.

²Indian Institute of Technology Gandhinagar Palaj, Gandhinagar 382355, India.

³Institute of Applied Physics of the Russian Academy of Sciences 46 Ul'yanov str., 603950 Nizhny Novgorod, Russia.

⁴Aryabhata Research Institute of Observational Sciences, Manora Peak, Nainital 263002, India.

Accepted 2023 September 28. Received 2023 September 27; in original form 2023 May 10

ABSTRACT

We present an analysis of the dense gas structures in the immediate surroundings of the massive young stellar object (MYSO) W42-MME, using the high-resolution ($0''.31 \times 0''.25$) ALMA dust continuum and molecular line data. We performed a dendrogram analysis of H^{13}CO^+ (4–3) line data to study multi-scale structures and their spatio-kinematic properties, and analyzed the fragmentation and dynamics of dense structures down to ~ 2000 AU scale. Our results reveal 19 dense gas structures, out of which 12 are leaves and 7 are branches in dendrogram terminology. These structures exhibit transonic–supersonic gas motions ($1 < \mathcal{M} < 5$) with overvirial states ($\alpha_{\text{vir}} \geq 2$). The non-thermal velocity dispersion–size relation ($\sigma_{\text{nt}} - L$) of dendrogram structures shows a weak negative correlation, while the velocity dispersion across the sky (δV_{lsr}) correlates positively with structure size (L). Velocity structure function ($S_2(l)^{1/2}$) analysis of H^{13}CO^+ data reveals strong power-law dependencies with lag (l) up to a scale length of $\lesssim 6000$ AU. The mass-size ($M - R$) relation of dendrogram structures shows a positive correlation with power-law index of 1.73 ± 0.23 , and the leaf L17 hosting W42-MME meets the mass-size conditions for massive star formation. Blue asymmetry is observed in the H^{12}CO^+ (4–3) line profiles of most of the leaves, indicating infall. Overall, our results observationally support the hierarchical and chaotic collapse scenario in the proximity of the MYSO W42-MME.

Key words: Interstellar Medium (ISM), Nebulae – ISM: kinematics and dynamics – galaxies: star formation — stars: massive – HII regions

1 INTRODUCTION

Massive stars ($M > 8 M_{\odot}$) typically form in giant molecular clouds (GMCs), which are the largest known complexes of molecular gas and dust in our galaxy. Unlike the low-mass stars, where clear evolutionary steps have been established through theory and observations (e.g., Shu et al. 1987; McKee & Ostriker 2007), the evolution of young massive stars has no well-defined stages (Motte et al. 2018). Recent theoretical and numerical simulations have shown that the mass of newly formed stars is determined not only by small-scale mass accretion but also by large-scale, filamentary mass inflow/accretion (e.g., Padoan et al. 2020), which agrees with recent multi-scale and multi-wavelength observations (e.g., Yuan et al. 2017; Dewangan et al. 2022b; Liu et al. 2022a; Li et al. 2022;

Xu et al. 2023; Liu et al. 2023). The low efficiency in star formation (around 1–2% in a single free-fall time scale of a cloud; e.g., Myers et al. 1986; Krumholz & McKee 2005; Vutisalchavakul et al. 2016; Kim et al. 2021) hints that the turbulence and magnetic fields slow down the gravitational collapse of molecular clouds (e.g., Myers & Goodman 1988; Vazquez-Semadeni et al. 2000; Bergin & Tafalla 2007; Hennebelle & Inutsuka 2019; Krumholz & Federrath 2019). Also, the profound work by Larson (1981) and follow up studies (e.g., Solomon et al. 1987; Goodman et al. 1998; Bolatto et al. 2008; Heyer et al. 2009; Cen 2021; Zhou et al. 2022, and references therein) suggest that turbulence dissipates into the smaller regions of clumps and cores which are more prone to gravitational collapse leading subsequent star formation. Consequently, the non-thermal motions on the scale of dense star-forming cores (~ 0.1 pc) can be sonic (e.g., Myers & Goodman 1988; Caselli et al. 2002), which agrees with the observations of filamentary, low-mass star-

*Email: naval@prl.res.in, bhadriaval@gmail.com

forming clouds (Hacar & Tafalla 2011; Hacar et al. 2017; Pineda et al. 2015). However, the nature of turbulence in the massive star-forming clumps/cores remains ambiguous, as previous studies have shown a range of supersonic ($\mathcal{M} \geq 2$; e.g., Carolan et al. 2009) to subsonic ($\mathcal{M} \leq 1$; e.g., Li et al. 2020) non-thermal velocity dispersion.

Recent observations hint that the massive star formation (MSF) involves simultaneous onset of multiple physical processes from the scales of molecular clouds (>10 pc) to cores (≤ 0.1 pc; Fukui et al. 2021a; Hacar et al. 2022; Bhadari et al. 2022, and references therein). This may be possible because of the hierarchical fragmentation process (i.e., fragmentation of cloud to high density structures of filaments, clumps and cores) that is primarily driven by the combined effect of turbulence and gravity (e.g., Goodman et al. 2009; Inoue & Fukui 2013; Padoan et al. 2020; Fukui et al. 2021b,a; Federrath et al. 2021). The gas motions of molecular clouds are coherent across scales of >10 pc to ~ 0.1 pc, and exhibit a universal velocity dispersion-size scaling relation observed in different environments (e.g., Solomon et al. 1987; Zhou et al. 2022; Liu et al. 2022b). This indicates that the dense fragments at different spatial scales are kinematically connected (Rosolowsky & Leroy 2006; Rosolowsky et al. 2008; Goodman et al. 2009). In context to recent studies, the velocity dispersion-size relation appears to follow the Larson (1981) first relation of $\Delta V \propto R^{0.38}$ with power law index in the range of 0.3–1.2 for larger scales (100–0.1 pc) (e.g., Fuller & Myers 1992; Goodman et al. 1998; Heyer et al. 2009; Falgarone et al. 2009; Cen 2021; Izquierdo et al. 2021), where ΔV and R are the velocity dispersion and radius/size of cloud. The observed relation resembles the energy cascade in turbulent systems, indicating that turbulence dissipates from larger spatial scales to smaller ones. The other two Larson’s relations imply the virial equilibrium with the constant surface densities over all the spatial scales. However, at the smaller scales of clouds where the density becomes high and multiple centers of collapse form, the role of both gravity and turbulence become important and hence at these scales the Larson’s relations are debatable (i.e., < 0.1 pc; Ballesteros-Paredes et al. 2007, 2011; Traficante et al. 2018a,b). As a result, the effect of gravity and turbulence during the early stages of star formation including the massive ones, is one of the current hot topics in star formation research (e.g., Ballesteros-Paredes et al. 2018; Federrath et al. 2021, and references therein).

The recent advancement of observational facilities such as the Atacama Large Millimeter/submillimeter Array (ALMA) has provided a great insights to the core scales in star-forming regions. It extends our limit of studying the gas kinematics of dense structures from cloud to the core scales. This paper primarily makes use of the ALMA H^{13}CO^+ (4–3) data and presents a comprehensive study of the dense gas kinematics of a small area (0.304×0.181 pc²) in W42 region (distance ~ 3.8 kpc; see Dewangan et al. 2022b, and references therein), known to host a bipolar H II region and Class II 6.7 GHz methanol maser emission (MME; see Figure 1 in Dewangan et al. 2015b). The H II region is powered by an O5–O6 star (O5.5, hereafter; Blum et al. 2000), and the ionized and molecular gas have similar velocities of about 60 km s^{-1} , suggesting they are part of the same physical system (Quireza et al. 2006; Anderson et al. 2009; Dewangan et al. 2015b). The infra-red counterpart of 6.7 GHz MME in W42 (W42-MME, hereafter) is a rare young massive protostar (or massive young stellar object; MYSO hereafter), believed to be in an early evolutionary stage (Dewangan et al. 2015a, 2022b; De Buizer et al. 2022). It has a luminosity of approximately $4.5 \times 10^4 L_{\odot}$ and is located at the center of a parsec-scale bipolar outflow in H_2 image (see Dewangan et al. 2015a, for more

details). Figure 1a shows the ALMA 1.35 mm image of an extended area ($\sim 45'' \times 45''$) in the direction of W42-MME, which is further zoomed in to the $865 \mu\text{m}$ continuum image in Figure 1b. The positions of W42-MME and the O5.5 star are also marked. Recent high-resolution ($\sim 0''.3$) molecular line study based on the ALMA data shows that the dusty envelope (~ 9000 AU) surrounding W42-MME hosts at least five continuum peaks (Dewangan et al. 2022b). One of the major peaks associated with W42-MME shows the signature of bipolar outflow and a disk-like feature with velocity gradients. This study by Dewangan et al. (2022b) suggests that MYSO W42-MME gains mass from its disk and the dusty envelope simultaneously. In the larger physical extent of ~ 3 – 5 pc, these authors found the presence of hub-filament system (HFS) which hosts our target region of study at its central hub-region (~ 1 – 2 pc; see Figure 14 in Dewangan et al. 2022b). It is to be noted that both the main sequence O5.5 star and the MYSO belong to the hub region. The radio continuum emission is also observed at 6 cm wavelength in the target area (see Figure 1c in Dewangan et al. 2022b). Targeting such region for high-resolution multi-wavelength and multi-scale study provides us a comprehensive understanding of different factors involved in MSF from the molecular cloud (> 5 – 10 pc) to core scale (< 0.1 pc).

In this paper we primarily utilized the high-resolution ALMA H^{13}CO^+ data to study the physical and kinematic properties of immediate surroundings of MYSO W42-MME, including the dusty envelope. The paper is structured as follows: Section 1 serves as an introduction to the study, Section 2 provides the description of data used in this study, and Section 3 outlines the results obtained from dendrogram analysis. Finally we discuss the consequences of the derived results in Section 4 and summarize the outcomes in Section 5.

2 ALMA DATA SETS

This paper utilizes H^{12}CO^+ (4–3) ($\nu \sim 356.734$ GHz), H^{13}CO^+ (4–3) ($\nu \sim 346.998$ GHz), and CH_3CCH (21_K-20_K) ($\nu \sim 358.709$ – 818 GHz) data obtained from the ALMA in Band 7, acquired under project ID: #2018.1.01318.S (PI: Lokesh Kumar Dewangan). The observed data has a beam size of $0''.31 \times 0''.25$. The details of data acquisition and reduction are given in Dewangan et al. (2022b). Additionally, we have utilized the ALMA continuum data at $865 \mu\text{m}$ ($\nu \sim 346.5$ GHz) from Dewangan et al. (2022b), which has a similar resolution to that of the line data. Furthermore, the publicly available ALMA continuum map at 1.35 mm (resolution $\sim 1''.2 \times 1''.1$) is obtained from the ALMA science archive (project ID #2019.1.00195.L; PI: Molinari, Sergio). It is used to display the large area around W42-MME in Figure 1a. The high-resolution Very Large Telescope (VLT) NAOS-CONICA (NACO) NIR adaptive-optics image at K_s band ($\lambda = 2.18 \mu\text{m}$; resolution $\sim 0''.2$) is also utilized from Dewangan et al. (2015a, see more details in their paper).

We used the ALMA $\text{H}^{12}\text{CO}^+/\text{H}^{13}\text{CO}^+$ data to analyze the dense gas kinematics and the CH_3CCH (21_K-20_K) data to estimate the temperature of the dense gas. In addition, we employed dust continuum maps to determine the mass of dense gas.

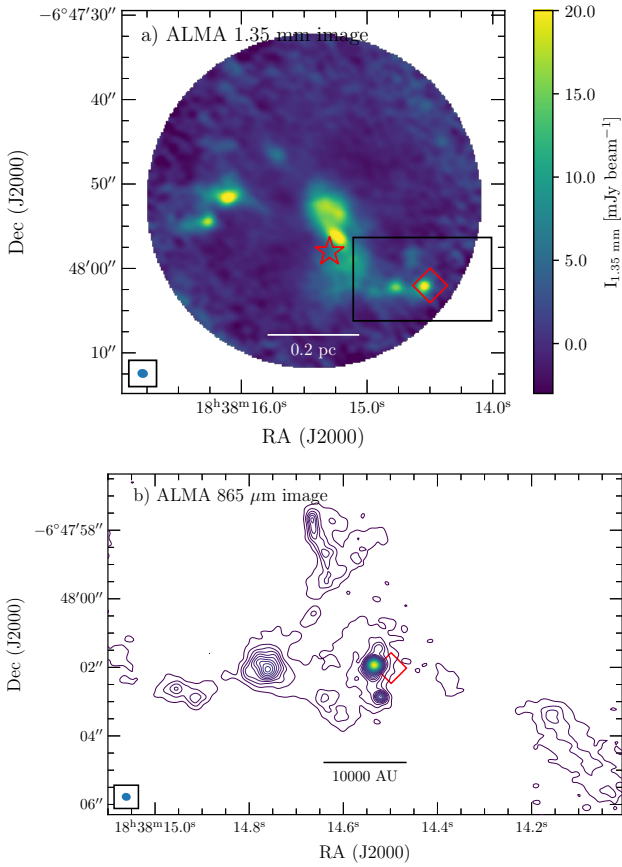


Figure 1. a) ALMA 1.35 mm continuum emission map of an extended area around W42-MME. b) ALMA 865 μm dust continuum contour map of an area marked by rectangular box in panel “(a)”. The emission contour ranges from 0.4 to 43.55 mJy beam^{-1} (i.e., maximum intensity of the image) in steps of 0.43 mJy beam^{-1} . The positions of the 6.7 GHz MME and ionizing O-type star are marked by diamond and star symbols, respectively. The scale bars are shown at $d = 3.8$ kpc. The beam size of ALMA images are shown in bottom-left corner.

3 RESULTS

3.1 Dendrogram analysis of ALMA H^{13}CO^+ (4–3)

Dendrogram analysis is a powerful tool for studying the physical properties of hierarchical structure of star-forming molecular clouds. The dendrogram methodology, as described by Rosolowsky et al. (2008), involves creating a tree diagram that characterizes emission structures based on their three-dimensional intensity isocontours. This method allows us to extract the emission structures at different spatial scales in a position-position-velocity (p - p - v) space, which is critical for understanding the complex interplay between dense gas kinematics, temperature, and star formation (e.g., Shetty et al. 2012). The dendrogram is a hierarchical tree structure composed of two components: branches and leaves. Branches can split into multiple sub-structures (i.e., new branches and leaves), while leaves have no sub-structures. In this context, leaves (i.e., potential star-forming cores) represent the small-scale, bright structures at the tips of the tree that do not break down into further sub-structures. Branches (i.e., clumps), on the other hand, represent the large-scale, fainter structures lower in the tree that do break down into substructures.

To perform the dendrogram analysis, we utilized the python-based *astrodendro*¹ package. This tool offers a method for determining the dendrogram structures within astronomical data in either 2D position-position (p - p) maps or 3D p - p - v data cubes. The algorithm *astrodendro* works by dividing the p - p - v data cube into a set of regions based on the distribution of intensity. The regions are then grouped together based on the specified similarity criterion, such as a threshold emission. This grouping process is repeated recursively until all of the regions are grouped together into a single structure. The result of this process is a tree-like diagram, or dendrogram, which represents the hierarchical structure of the cloud.

3.1.1 Structure Identification and H^{13}CO^+ (4–3) moment maps

We applied the dendrogram analysis to the ALMA H^{13}CO^+ (4–3) data (in p - p - v space) on 0.304×0.181 pc^2 area of our target region (see area footprint in Figure 1b) in order to extract the hierarchical structure of the dense gas in the W42-MME region. The ALMA H^{13}CO^+ (4–3) line emission reveals mostly single peaked profiles toward the entire area of our target site, which is noticeable from Figure 2 presenting the overlay of averaged H^{13}CO^+ spectra over the regular grids of $0''.864 \times 0''.432$ toward our target site. The background image is H^{13}CO^+ integrated intensity map (see following text in this Section). The hierarchical tree diagram of dendrogram structures is extracted and is shown in Figure 3. This exercise allowed us to identify and classify the different scales of the dense gas emission in the cloud, from the small-scale structures (i.e., ≤ 0.01 pc) to relatively larger structures (≥ 0.05 pc). Below are the steps we followed to identify the dendrogram structures.

To enhance the performance of the dendrogram algorithm, pixels with noise levels lower than three times the local noise level were masked out. By analyzing the source/emission free individual velocity channels, we found that the local noise (or rms) varies from 1.6 to 3 mJy beam^{-1} with mean value of $\sigma_{\text{rms}} = 2.3$ mJy beam^{-1} . The estimated σ_{rms} value is close to that of obtained by Dewangan et al. (2022b) for a spectral resolution of 0.242 MHz. We therefore masked out the noisy pixels which are below $3\sigma_{\text{rms}}$ ($= 7$ mJy beam^{-1}) from the H^{13}CO^+ (4–3) data cube. This step is equivalent to set the “min_value” parameter of *astrodendro* algorithm, which signifies the minimum emission in the Dendrogram tree structure. We further specified the values of other two crucial parameters used as inputs for the *astrodendro* algorithm. These are “min_delta”, and “min_npix”. The parameter “min_delta”, that indicates the minimum difference between two intensity peaks such that they can be considered as separate structures, was set to be $1\sigma_{\text{rms}}$ ($= 2.3$ mJy beam^{-1}). The another parameter “min_npix” indicates the minimum number of spatial-velocity pixels required for a leaf structure to be considered as independent entity. We have chosen this value such that a dendrogram structure contains at least two synthesized beam of ALMA H^{13}CO^+ (4–3) data. This is essential in order to measure the structure size and line width (Rosolowsky & Leroy 2006). Thus, “min_npix” was set to be 74 pixels (1 pixel = $0''.048$). The algorithm ultimately identified 19 structures including 7 branches and 12 leaves. Figure 3 displays the branches and leaves structures in the dendrogram tree.

We have superimposed the spatial distribution of the identified leaf structures on the peak intensity (F_{peak}) map of the ALMA H^{13}CO^+ (4–3) data, as shown in Figure 4a. Each leaf structure is marked with its corresponding structure ID. The map provides

¹ <https://dendrograms.readthedocs.io/en/stable/index.html>

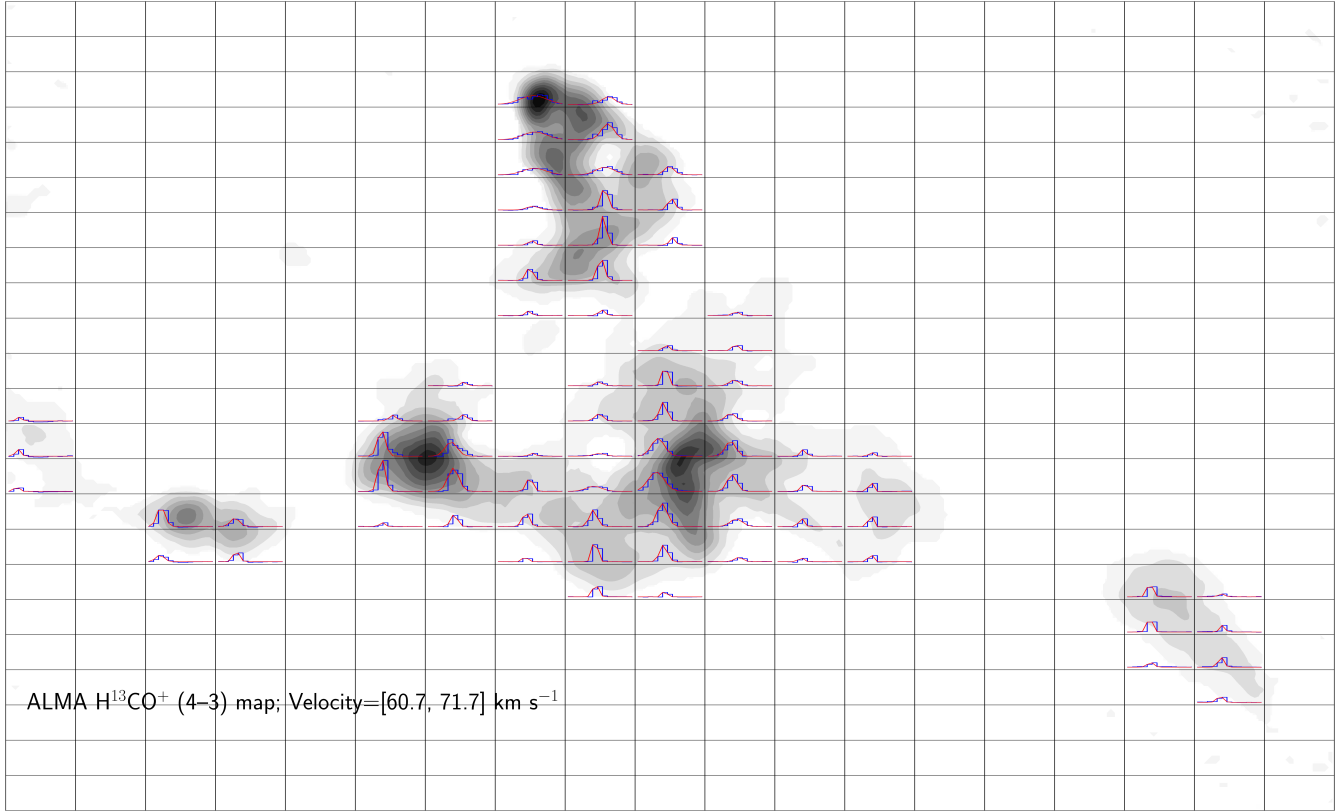


Figure 2. ALMA H^{13}CO^+ (4–3) moment-0 map overlaid with the averaged velocity profiles extracted along the regular grids of size $0''.864 \times 0''.432$. The extent of figure is identical to that of the Figure 1b. Profiles in red are the 1-D Gaussian fit to the observed spectra (in blue). The y-scale ranges from -2.94 to $89.14 \text{ mJy beam}^{-1}$, while x-scale is V_{LSR} from 60.73 to 71.70 km s^{-1} .

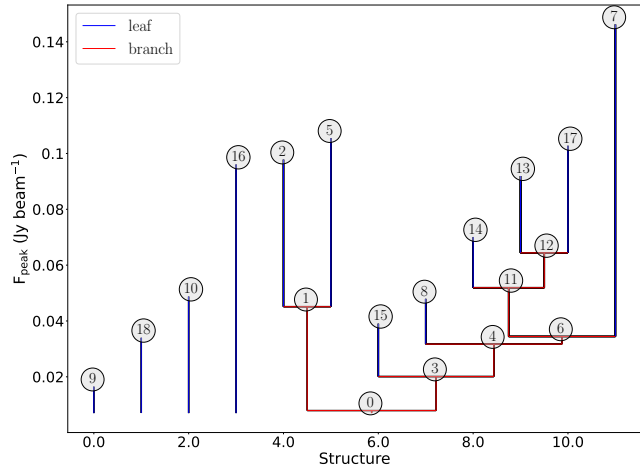


Figure 3. Dendrogram tree of hierarchical structures identified from ALMA H^{13}CO^+ (4–3) data. The leaves and branches are marked in the tree structure (see also Figure 4).

a snapshot of the overall peak intensity distribution of the dense molecular gas. The dendrogram methodology can be understood by comparing the dendrogram tree structure (see Figure 3) and the peak intensity map (see Figure 4a). Figure 4b presents the peak velocity (V_{peak}) map of the ALMA H^{13}CO^+ (4–3) data which infers the gas velocity at peak intensity. A coherent velocity structure is noticeable along the $\text{Dec} \sim -06^\circ 47'' 02'$ at velocity of $[62, 66] \text{ km}$

s^{-1} . The northern structure, however, is seen at the redshifted velocities (see more discussion in Section 4). Figure 4b also shows the overlay of leaf structures on the V_{peak} map of H^{13}CO^+ emission, by their corrected sky-projected size. To infer the presence of point-like sources in our target area, we have displayed the VLT/NACO adaptive-optics K_s band image of our target region in Figure 4c and overlaid the footprints of leaves and branches. As can be seen in Figures 4a–c (for comparison see Figure 3), the central region is identified as dendrogram structure B0, which is separated from the other structures. This branch is further divided into 6 sub-branches and 8 leaves. Notably, leaf L17 belongs to the W42-MME, which has been previously described in (Dewangan et al. 2022b). Based on the VLT/NACO adaptive-optics K_s band image, here we note that most of the point sources do not lie in the direction of identified structures. In other words, the turbulence in most of the dendrogram structures do not seem to be influenced by the presence of point-like sources.

We have also computed the moment statistics of ALMA H^{13}CO^+ (4–3) data. In millimeter–radio astronomy, moment maps provide a way to characterize the distribution of emission over a region of the sky. The first three moments i.e., moment-0; $M_0 = \int I_\nu dv$, moment-1; $M_1 = \frac{\int \nu I_\nu dv}{M_0}$, and moment-2; $M_2 = \sqrt{8 \ln 2} \times \sqrt{\frac{\int I_\nu (\nu - M_1)^2 dv}{M_0}}$, refer the integrated intensity over spectral/velocity axis, intensity weighted centroid velocity, and intensity weighted velocity dispersion (full width at half maximum (FWHM)), respectively. Figure 5a presents the M_0 map of ALMA H^{13}CO^+ emission in the direction of our target region, inferring the overall inten-

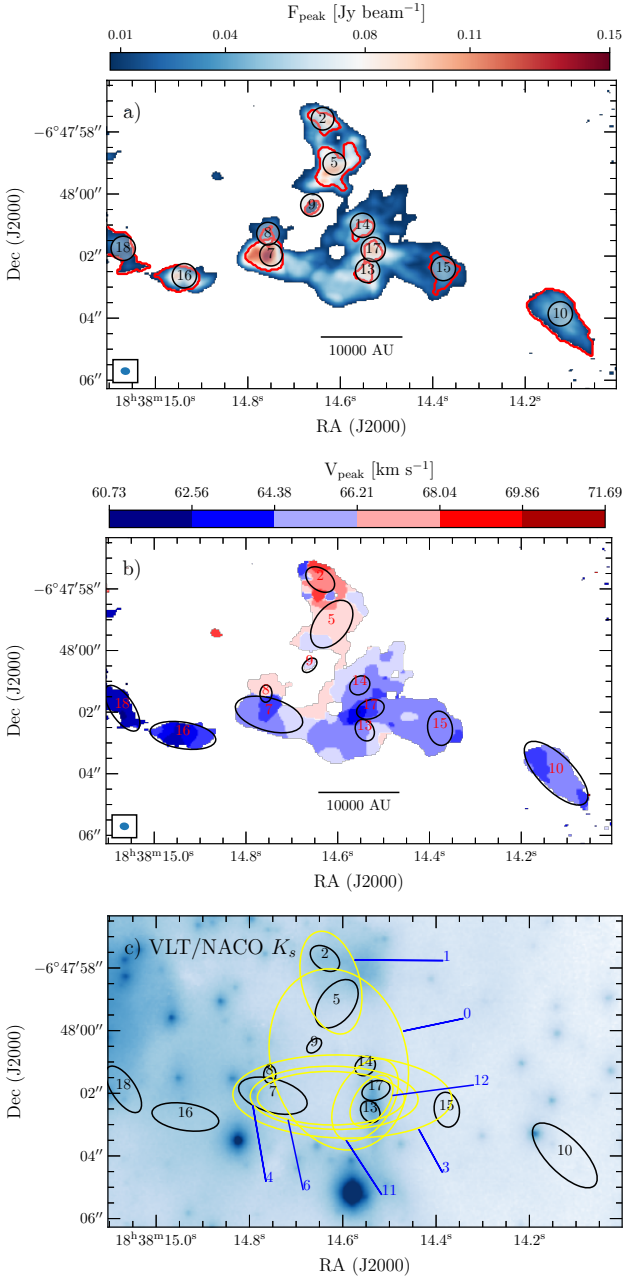


Figure 4. a) ALMA H^{13}CO^+ (4–3) peak intensity map of region hosting W42-MME. The *astrodendro* identified leaf structures are overlaid and shown with contours and associated IDs, respectively. (b) Peak velocity map derived using ALMA H^{13}CO^+ (4–3) emission. (c) VLT/NACO adaptive-optics K_s band image. In panels “b” and “c”, the ellipses approximating the leaves (in black) and branches (in yellow) are shown. The structure ID for leaves and branches is displayed.

sity/density distribution of dense gas. The velocity range of [60.73, 71.70] km s^{-1} has been used for generating the M_0 map and identifying the dendrogram structures in p - p - v space. Figure 5b shows the M_1 map providing the information of gas velocity distribution. The M_2 map of extended area around W42-MME is shown in Figure 5c, revealing the ALMA H^{13}CO^+ FWHM linewidth distribution. The high value of velocity dispersion in the northern knot (leaf ID L2) is possible because of the presence of multiple velocity components (see blue spectra in Figure 2). However in the direction of W42-

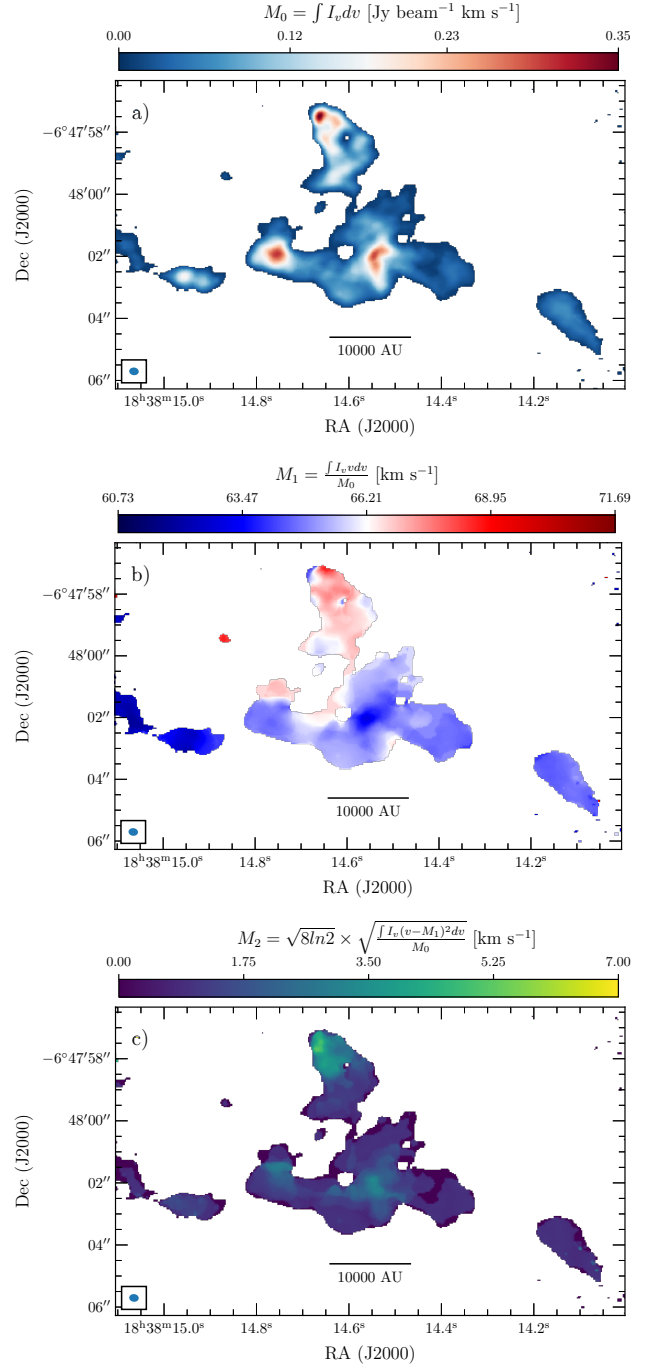


Figure 5. ALMA H^{13}CO^+ emission map of a) integrated intensity in the velocity range of [60.73, 71.70] km s^{-1} (moment-0 map), b) intensity weighted velocity (moment-1 map) and b) intensity weighted FWHM velocity dispersion (moment-2 map) toward region hosting W42-MME.

MME (leaf ID L17) and other leaves (ID L8 and L13), the high-dispersion value is observed regardless of the absence of multiple velocity components in H^{13}CO^+ spectra (see Figure 2).

3.2 Physical parameters of dendrogram structures

The major and minor axis of dendrogram structures are related to *astrodendro* output parameters of “major_sigma” and “mi-

nor_sigma", which represent the 2nd spatial moments along longer and shorter direction, respectively. To obtain the physical extension of dendrogram structures (or major axis \times minor axis), we need to multiply the outputs (i.e., "major_sigma" and "minor_sigma") by $\sqrt{8 \ln 2}$. We have also taken account of the filling factor (f) as discussed in Liu et al. (2022b). In other words, the *astrodendro* derived major and minor axis are less by a factor of $f = \sqrt{A_{\text{exact}}/A_{\text{ellipse}}}$, where A_{exact} and A_{ellipse} are the exact and calculated areas of Dendrogram structures in the sky plane (see also Rosolowsky et al. 2008; Liu et al. 2022b).

Table 1 lists the physical parameters of all identified structures, including structure ID, sky coordinates, integrated flux (F^{int}), structure size (major axis(") \times minor axis(")), structure length (L), position angle (PA); measured counter-clockwise from the RA axis), gas kinetic temperature (T_{kin}), weighted mean velocity ($\langle V_{\text{lsr}} \rangle$), velocity variation (δV_{lsr}), observed weighted mean velocity dispersion ($\langle \sigma_{\text{obs}} \rangle$), non-thermal velocity dispersion ($\langle \sigma_{\text{nt}} \rangle$), three-dimensional (3D) Mach number (M_{3D}), and the number of ALMA beams (N) that can fit within each structure. The estimation of T_{kin} is presented in Section 3.2.1. We have also computed the gas mass (M_{S}), virial mass (M_{vir}), virial parameter (α_{vir}), and gas density (n) of each dendrogram structure in Section 3.2.2.

We estimated the size of dendrogram structures by taking the geometric mean of corrected major and minor axes using the formula

$$L(\text{AU}) = D(\text{pc}) \sqrt{\text{major axis}(\prime) \times \text{minor axis}(\prime)}, \quad (1)$$

where $D(= 3.8 \times 10^3)$ pc is the distance of W42. The $\langle V_{\text{lsr}} \rangle$ represents the error-weighted mean velocity and is estimated using the M_1 map (see Figure 5b) and the corresponding uncertainty map. Similarly, the weighted line-of-sight velocity dispersion/linewidth, $\langle \sigma_{\text{obs}} \rangle$, is inferred from the M_2 map (see Figure 5c) and the respective error map. The uncertainties in the M_1 and M_2 maps are derived using Equations 5 and 6 from Teague (2019, not shown here). The final error in the mean of a parameter, denoted as P (i.e., V_{lsr} or σ_{obs}), is computed as :

$$\Delta \langle P \rangle = \frac{1}{k} \sqrt{\sum_i^k \Delta p_i^2}, \quad (2)$$

where Δp_i and k are the uncertainty in measurements of P at i^{th} pixel and the total number of pixels within the footprint of dendrogram structures, respectively. The velocity variation, δV_{lsr} , representing the plane-of-sky velocity dispersion, is estimated as the standard deviation of V_{lsr} within the structure. Its uncertainty is given by $\delta V_{\text{lsr}} / \sqrt{2(k-1)}$.

Additionally, we derived the non-thermal velocity dispersion as:

$$\langle \sigma_{\text{nt}} \rangle = \sqrt{\langle \sigma_{\text{obs}}^2 \rangle - \sigma_{\text{th}}^2}, \quad (3)$$

where σ_{th} is the thermal velocity dispersion for dendrogram structure, and is given by

$$\sigma_{\text{th}} = \sqrt{\frac{k_B T_{\text{kin},i}}{\mu m_{\text{H}}}}. \quad (4)$$

In Equation 4, $\mu=30$ is the molecular weight of the H^{13}CO molecule, m_{H} is the mass of atomic hydrogen (approximating to proton mass), k_B is the Boltzmann constant, and $T_{\text{kin},i}$ is the gas kinetic temperature of the i^{th} structure derived using CH_3CCH (21 $_K$ –20 $_K$) emission (see Section 3.2.1). The value of sound speed c_s in

a medium is influenced by all the gas particles present in it. This can be determined using Equation 4 with a mean molecular weight per free particle of $\mu=2.37$ (Kauffmann et al. 2008). The 3D Mach number, M_{3D} , is estimated by $\sqrt{3}\sigma_{\text{nt}}/c_s$.

3.2.1 Dense gas temperature (T_{kin}) estimation

Previous studies show that the low excitation level (e.g., $J=5-4$) transitions from CH_3CCH molecule give a good estimate of the kinetic temperature at gas density of $\sim 10^{3-4} \text{ cm}^{-3}$ (Askne et al. 1984; Bergin et al. 1994). However, the higher level transitions can trace gas density $\geq 10^{5-6} \text{ cm}^{-3}$ (e.g., Aladro et al. 2011; Santos et al. 2022), which can be used to estimate the gas temperature of dense environment as traced by HCO^+ (4–3) transition with a critical density of (i.e., $\sim 3.5 \times 10^6$ to $2 \times 10^6 \text{ cm}^{-3}$ for the temperature range of 10–100 K, respectively; Shirley 2015). Therefore, we utilized the ALMA Band 7 CH_3CCH data to estimate the gas kinetic temperature (T_{kin}) of dendrogram structures identified in H^{13}CO^+ (4–3) transition. The observed data contains five components of the CH_3CCH (21–20) K-ladder with $K=0-4$, and we generated the corresponding averaged spectrum for each dendrogram leaf and branch structure. The rotational temperatures for the dendrogram leaf and branch structures are determined using these transitions. The spectrum and corresponding rotation diagrams of leaf L17 are presented in Figure 6. The diagram plots the values proportional to natural logarithm of the measured integrated line intensity, S_{ν} , against the upper energy level E_u of specified molecule. The y -axis corresponds to a parameter defined by the quantum numbers J and K , the transition frequency ν , the dipole moment μ , the degeneracy g_K associated with the internal quantum number K , and the statistical weight g_I associated with the nuclear spin. The slope a of the fitted straight line, $y = ax + b$, is related to the kinetic temperature, $T_{\text{kin}} = -\frac{1}{a}$, while the uncertainty in the estimation of T_{kin} is $\Delta T_{\text{kin}} = \frac{\Delta a}{a^2}$.

The temperature estimates for leaf structures ranged from 33 to 70 K, with the mean (median) values of 54.27 (61.84) K, while for branches the range is [56.08, 68.23] K with mean (median) value of 60.53 (58.94) K. It is important to note that in the case of leaves L9, L16, and L18, weak emission is observed in CH_3CCH (21–20) line, which made it difficult to define T_{kin} of these structures.

3.2.2 Dense gas mass (M_{S}) and virial parameter (α_{vir}) estimation

The dust/gas mass can be estimated from the knowledge of the dust emission in the interstellar medium (ISM). With the assumption of spherical dust grains and the optically thin dust emission as a modified black body emission in the Rayleigh-Jeans limit, the gas mass can be estimated as:

$$M_{\text{S}} = \frac{F_{\nu} D^2 R_t}{B_{(\nu, T_d)} k_{\nu}}, \quad (5)$$

where F_{ν} , D , $B_{(\nu, T_d)}$, R_t , and k_{ν} are total integrated flux at observing frequency ν , distance of object, Planck function at dust/gas temperature T_d , gas-to-dust mass ratio, and dust absorption coefficient, respectively.

By adding up the emission inside the boundary of each dendrogram structure, we calculated F_{ν} at $\nu = 346.58$ GHz (or 865 μm) for each one. We derived the k_{ν} by adopting a relation $k_{\nu} = 10 \left(\frac{\nu}{1.2(\text{THz})} \right)^p$, where $p = 1.5$ is adopted for all the dense cores

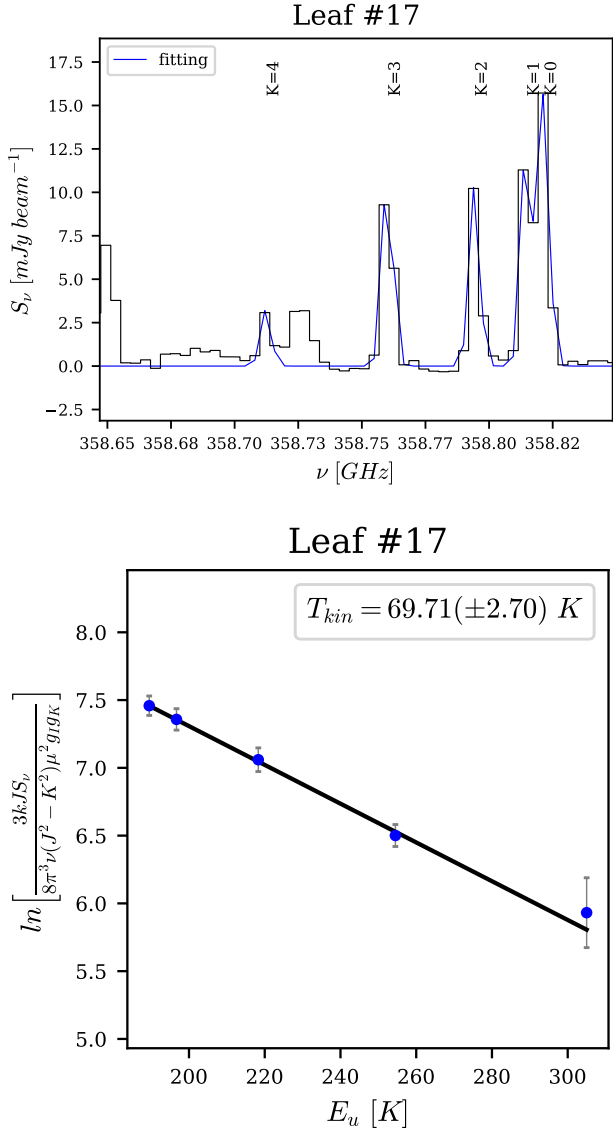


Figure 6. *Upper panel:* Averaged CH_3CCH ($21_K\text{--}20_K$) spectra (in black) and best fit model of CH_3CCH lines (in blue) for Dendrogram leaf L17. *Lower panel:* CH_3CCH rotation diagrams of leaf L17 (see text for details). A best fit line to the 5 CH_3CCH transitions is shown and corresponding T_{kin} is labeled.

Figures 8d–8i display the kinematic properties of dendrogram structures. The weighted mean velocity of leaves and branches (see Figure 8d) are found to be similar with a value of $\sim 65 \text{ km s}^{-1}$. However, the branches show narrower distribution (range = $[64.53, 66.65] \text{ km s}^{-1}$) compared to leaves (range = $[62.37, 67.17] \text{ km s}^{-1}$). This is possible because the fewer leaves that are separated from the central zone (i.e., leaves L10, L16, and L18; see Figure 4), are identified at lower velocities and do not have their parent branches. A clear separation in the δV_{lsr} distribution for leaves and branches is noticeable in Figure 8e. The leaves, overall have less δV_{lsr} (range = $[0.05, 0.65] \text{ km s}^{-1}$, mean = 0.34 km s^{-1} , median = 0.35 km s^{-1}) compared to branches (range = $[0.56, 0.82] \text{ km s}^{-1}$, mean = 0.66 km s^{-1} , median = 0.67 km s^{-1}).

The histogram distribution of $\langle \sigma_{\text{obs}} \rangle$ and its non-thermal contribution, $\langle \sigma_{\text{nt}} \rangle$, for the identified structures are presented in Fig-

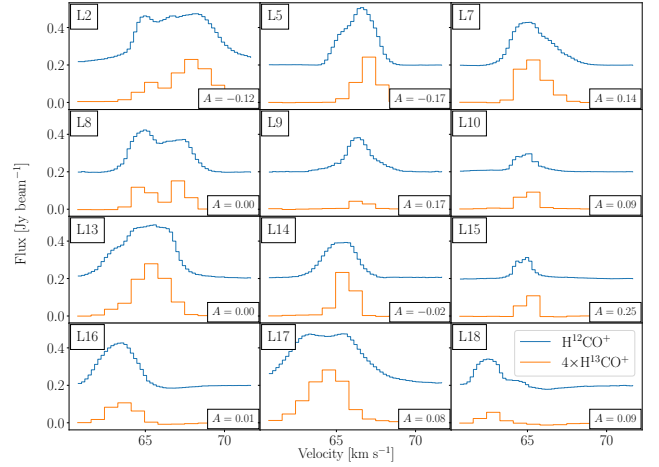


Figure 7. Averaged spectral profiles of dendrogram leaves. In each panel, the dendrogram leaf ID and asymmetry parameter (A) are labeled (see text for details). In all the panels, H^{12}CO^+ profiles are vertically offset by 0.2 Jy beam^{-1} , while the H^{13}CO^+ profiles are scaled up by a factor of 4.

ures 8f and 8g, respectively. The branches, overall, tend to have narrower velocity dispersion range (i.e., $\langle \sigma_{\text{obs}} \rangle$; range = $[0.42, 0.80] \text{ km s}^{-1}$, mean = 0.57 km s^{-1} , median = 0.54 km s^{-1}) compared to that of leaves (i.e., $\langle \sigma_{\text{obs}} \rangle$; range = $[0.19, 1.37] \text{ km s}^{-1}$, mean = 0.60 km s^{-1} , median = 0.50 km s^{-1}). The similar trend is reflected in the non-thermal velocity dispersion. For branches, the $\langle \sigma_{\text{nt}} \rangle$ ranges from 0.40 to 0.79 km s^{-1} with mean and median values of 0.56 km s^{-1} and 0.53 km s^{-1} , respectively, while for leaves, $\langle \sigma_{\text{nt}} \rangle$ is observed in the range = $[0.31, 1.37] \text{ km s}^{-1}$ with mean and median values of 0.69 km s^{-1} and 0.51 km s^{-1} , respectively. The α_{vir} distribution is shown in Figure 8h. Branches have less α_{vir} (mean = 3.89 and median = 2.92) compared to leaves (mean = 18.36 and median = 10.89). The distribution of $\mathcal{M}_{3\text{D}}$ (see Figure 8i) reveals the transonic–supersonic ($1 \leq \mathcal{M}_{3\text{D}} \leq 5$) nature of dendrogram structures. The mean (median) values of $\mathcal{M}_{3\text{D}}$ for leaves and branches are 2.69 (2.39) and 2.08 (2.04), respectively.

3.4 Line-width size ($\sigma - L$) relation

The linewidth-size ($\sigma - L$) relationship of the molecular clouds has been investigated extensively in the literature (see Section 1). Typically, this relationship is well described by a power law with an index ranging from 0.2 to 0.6 (Larson 1981; Solomon et al. 1987; Goodman et al. 1998; Heyer & Brunt 2004; Heyer et al. 2009; Falgarone et al. 2009; Hacar et al. 2016; Dewangan et al. 2019, 2022a), and is commonly known as first of the three ‘‘Larson’s Relations’’. Since the nature of turbulence and star formation is closely linked to these relationships, it is crucial to evaluate the $\sigma - L$ correlations in various environments and scales to gain a comprehensive understanding of the star-forming regions. To understand the nature of turbulence in a star-forming environment, we investigated the $\sigma_{\text{nt}} - L$ relationship of regions in the immediate vicinity of W42-MME (see Figure 1b). This is of the type-4 $\sigma - L$ relation as discussed by Goodman et al. (1998). Earlier, Goodman et al. (1998) devised four types of $\sigma - L$ relations, which are the combinations of line tracers (i.e., single or multiple) and the target of interest (i.e., single or multiple molecular clouds). In this way type-1 relation is for multitracer, multcloud intercomparison, type-2 is for single-tracer, multcloud intercomparison, type-3 is for multitracer study of a single cloud, and type-4 indicates the single-tracer study of a

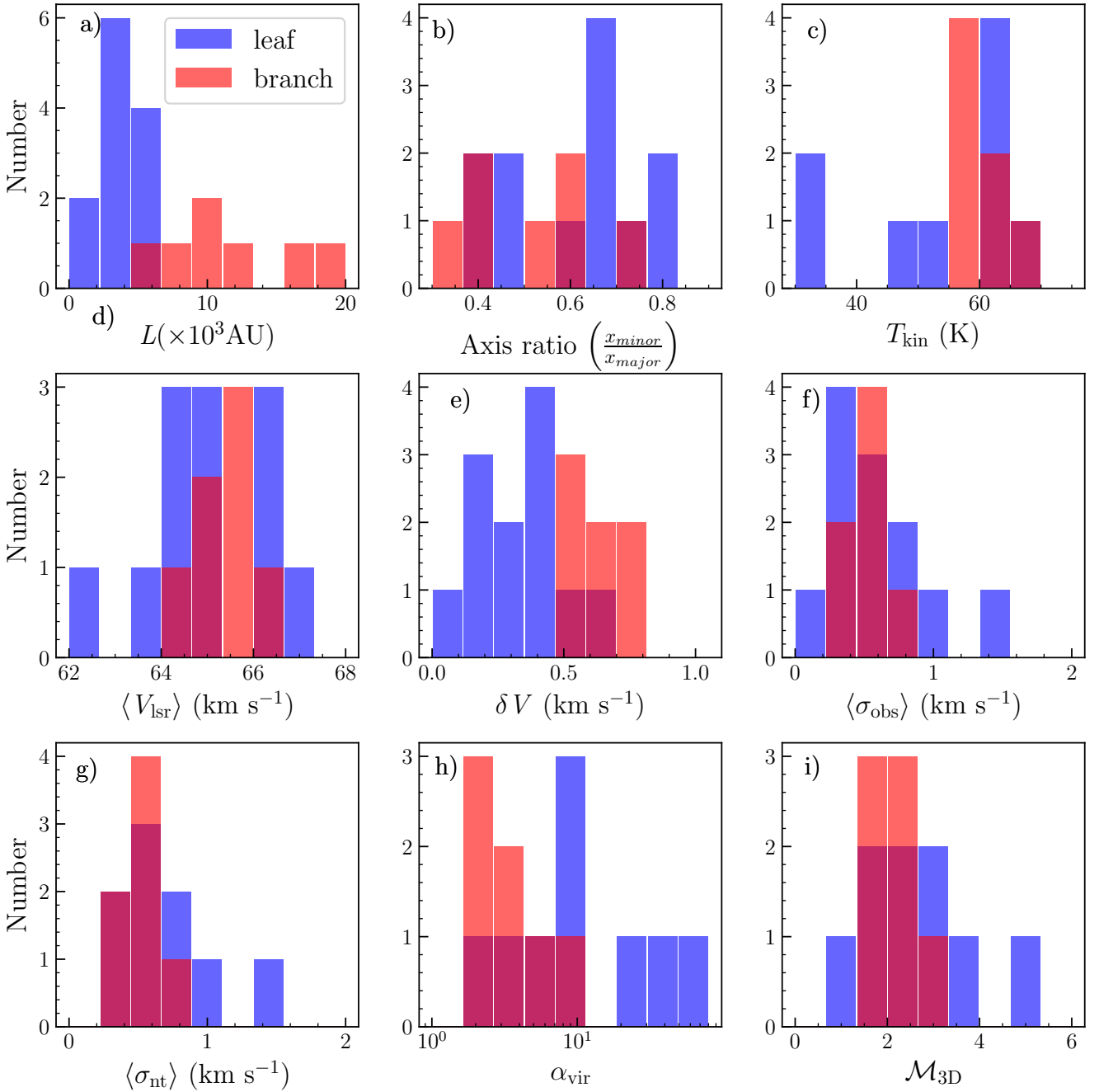


Figure 8. Histograms of different properties of *astrodendro* identified structures. These include structure size (L in AU), axis ratio ($\frac{\text{minor axis}}{\text{major axis}}$), mean velocity ($\langle V_{\text{lsr}} \rangle$), velocity variation (δV_{lsr}), observed mean velocity dispersion ($\langle \sigma_{\text{obs}} \rangle$), non-thermal velocity dispersion ($\langle \sigma_{\text{nt}} \rangle$), gas kinetic temperature (T_{kin}), virial parameter (α_{vir}), and Mach number ($\mathcal{M}_{3\text{D}}$). Histograms in blue and red correspond to leaf and branch structures, respectively.

single cloud. Here we study this relation by two approaches, one using dispersion–size plot for dendrogram structures, and other by estimating the velocity structure function (VSF) for the entire region of study.

3.4.1 Scaling relations from Dendrogram Structures

In the analysis below, we explore two scaling relationships concerning the dendrogram density structures (i.e., leaves and branches) identified in W42 region. Two parameters, σ and δV_{lsr}

are used to measure internal gas motions (e.g., Storm et al. 2014; Liu et al. 2022b). The parameter σ indicates the internal gas motion in the direction of an individual structure (line-of-sight velocity dispersion or linewidth), while δV_{lsr} traces the gas motion across different directions within the structure (plane-of-sky velocity dispersion). At the cloud scale (>10 pc), the choice of these parameters is insignificant as these two parameters are similar and commonly trace the internal gas motion of the cloud. However, at smaller scales (<0.1 pc), local effects become more important and gas properties become distinguishable. Therefore, in partic-

ular, we are interested in the scaling relationships of $\delta V_{\text{lsr}} - L$ and $\sigma_{\text{nt}} - L$. Figure 9a presents the $\delta V_{\text{lsr}} - L$ plot for the identified dendrogram structures. The best fit power-law has the form $\delta V_{\text{lsr}} = (0.20 \pm 0.06) \times L^{0.46 \pm 0.14}$, which closely follows the generalized Larson’s law with power-law scaling exponent of ~ 0.5 at a constant column density of $\sim 10^{23} \text{ cm}^{-2}$ (e.g., Heyer & Brunt 2004). We have also marked the lines of constant column density in Figure 9 following the equation, $\sigma = \sqrt{2G\Sigma L}$, where Σ is the column density, G is the universal gravitational constant, and L is the structure size (see Ballesteros-Paredes et al. 2011, for details). This equation is valid if the collapsing scenario is applicable to all scales within the molecular cloud and the non-thermal motions are of gravitational origin. However, such equation is also applicable for the case of virial equilibrium, with a difference by a factor of $\sqrt{2}$ less (see more details in Ballesteros-Paredes et al. 2011). The power-law exponent in the $\delta V_{\text{lsr}} - L$ relation for branch structures is found to be shallower with the value of 0.27 ± 0.10 compared to the global trend. We have marked the footprint of Larson’s law with the scaling coefficient ranging from 0.08 to 0.8 by shaded area in Figure 9.

We further estimated the Pearson Correlation Coefficient (PCC) which is a measure of linear correlation between two sets of data. The PCC correlation coefficient r indicates the strength of the linear relationship, while the significance is measured by the probability value p . It is to be noted that the r ranges from -1 to $+1$ signifying the strong anti-correlation ($r = -1$), no correlation ($r = 0$), and strong positive correlation ($r = +1$), respectively. The smaller p value indicates more significant relationship. In general $p < 0.05$ signifies statistically significant correlation. For $\delta V_{\text{lsr}} - L$ plot, we obtained the r -value and p -value of 0.69, and 2.92×10^{-3} , respectively. This indicates the positive correlation between δV_{lsr} and (L) of dendrogram structures.

Figure 9b shows the $\sigma_{\text{nt}} - L$ plot for the identified structures. This plot overall shows negative trend with scaling exponents of -0.31 ± 0.14 , which is obtained from the best fit power-law over all the identified structures. With $p = 0.056$, the correlation coefficient $r = -0.4$ between σ_{nt} and L is marginally statistically significant. In $\sigma_{\text{nt}} - L$ plot, a steeper negative trend with a power-law exponent of -0.55 ± 0.06 is found for the branch structures only. The PCC p -value of 2.04×10^{-3} with $r = -0.93$ suggests its statistical significance. The possible origin of these outcomes are discussed in Section 4.

3.4.2 Velocity Structure Function

An important statistical description of interstellar turbulence or the gas dynamics can be inferred by the generalized VSF (e.g., Miesch & Bally 1994; Heyer & Brunt 2004; Chira et al. 2019)

$$S_p(l) = \langle (v(r) - v(r+l))^p \rangle, \quad (9)$$

where, l is known as lag (i.e., the spatial displacement between two points within a three dimensional volume), p is the order of VSF, and the average is taken out for the entire volume of the gas. The VSF is described as a power-law over a finite spatial range and often reframed as a power-law expression by taking p^{th} root; i.e., $S_p(l)^{1/p} = v_0 l^\gamma$, where v_0 is a scaling coefficient and γ is a scaling exponent (Heyer & Brunt 2004). In our analysis, we calculated the reframed 2^{nd} order structure function in velocity $\delta v = S_2(l)^{1/2}$ (e.g., Hacar et al. 2016; Dewangan et al. 2019) using H^{13}CO^+ (4–3) data of entire region of our study (see Figure 1b). In our calculations, we adopted only those data points which have peak intensities greater than $0.01 \text{ Jy beam}^{-1}$ and have velocity dispersion

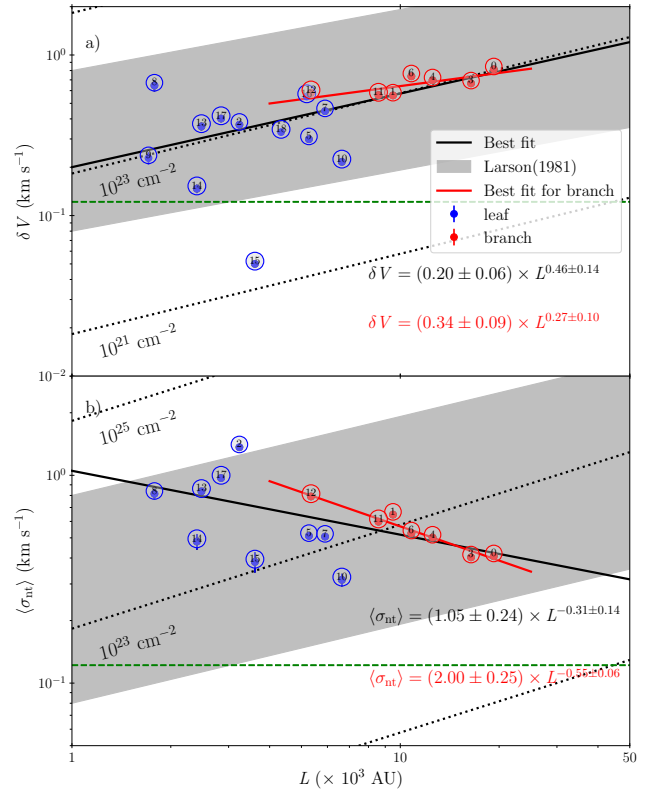


Figure 9. a) $\delta V_{\text{lsr}} - L$ plot. b) $\langle \sigma_{\text{nt}} \rangle - L$ plot. In both the panels, blue and red dots correspond to leaf and branch structures, respectively. We have also labeled the corresponding structure IDs. The best fit power-law for all the dendrogram structures (solid black line) and for only branch (red solid line) are displayed and labeled. The Larson (1981) relation ($L \propto \sigma^{0.38}$) is shown by shaded region with the coefficient range of 0.08 to 0.8 km s^{-1} . A green dashed line indicates thermal velocity dispersion of 0.129 km s^{-1} at mean gas temperature of dendrogram structures (i.e., 54 K). The dotted lines denote the lines of constant column density (see labels) if non-thermal motions are driven by the self gravity.

(FWHM) $< 2.5 \text{ km s}^{-1}$. Applying these conditions, the total number of data points were 7566 (i.e., $\sim 11\%$ of available points). We then estimated $S_2(l)^{1/2}$ using moment-1 map of H^{13}CO^+ and the total range of angular separations (i.e., $0''.05 - 19''.2$) were divided into sub-ranges (or lags) of $0''.13$ (or $\sim 500 \text{ AU}$ in spatial scale).

Figure 10 shows the $S_2(l)^{1/2} - l$ plot for H^{13}CO^+ (blue points) data. We have estimated the best fit power-law form of H^{13}CO^+ $S_2(l)^{1/2}$, which is obtained as $S_2(l)^{1/2} = (0.34 \pm 0.01) \times l^{0.40 \pm 0.01}$. Here we also note that there is no significant deviation in the $S_2(l)^{1/2}$ for H^{13}CO^+ and H^{12}CO^+ data (not shown here). In general, the $S_2(l)^{1/2}$ shows a linear trend in the spatial range within $\sim 6000 \text{ AU}$. The form of this linear trend is obtained as $S_2(l)^{1/2} = 0.23 \times l^{0.73 \pm 0.01}$, and is more steeper than the global trend with the form of $S_2(l)^{1/2} \propto l^{0.40 \pm 0.01}$. However, for larger separations ($\geq 6000 \text{ AU}$), the VSF rises slightly, and shows oscillatory behavior. This form of VSF is seen previously by other authors as well (e.g., Hacar et al. 2016; Dewangan et al. 2019, 2022a).

We have further investigated the variation of scaling coefficient (v_0) and scaling exponent (γ) for each dendrogram structure by computing the H^{13}CO^+ $S_2(l)^{1/2}$ in Figure 11. The histograms of γ for leaves and branches are shown in Figures 11a and 11b, respectively. Here we note that the γ is related to a linear regime in log-log plots of $S_2(l)^{1/2}$ of each structure (for comparison, see Figure 10).

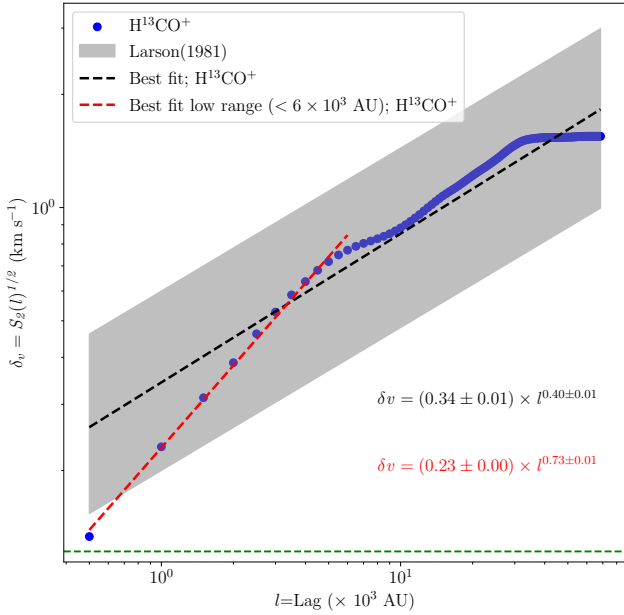


Figure 10. Structure function in velocity ($S_2(l)^{1/2}$) as a function of lag (l). The lag is sampled at the steps of 500 AU. A green dashed line indicates σ_{th} of 0.129 km s^{-1} at mean gas temperature of 54 K.

To perform such an analysis, we first masked out the area that does not include our region of interest (i.e., each dendrogram structure) and then computed the VSF. Due to the small structure sizes, here the VSF analysis is exempted from the conditions defined earlier (i.e., imposing cut-off in peak intensity and velocity dispersion). The total number of data points range from 62 to 943 for leaves, while for branches the data points were in the range of 675–5947. Figure 11c displays the distribution of γ and v_0 as a function of structure size. The distribution of γ is scattered for leaves, while it shows a negative trend for the branches. The distribution of v_0 is nearly constant for the branches.

3.4.3 Mass–size and density–size relations

To understand the nature of detected dendrogram structures, we computed the mass–size ($M - R$) and density–size ($n - R$) relations for the dendrogram structures in Figure 12. These relations can be derived from one another, implying that the column density of structures with various masses, sizes, and evolutionary states is constant. Collectively, these relations are known as Larson’s third relation. The $M - R$ relation has a best fit power-law with a form of $M \propto R_{\text{eff}}^{1.73 \pm 0.23}$, where R_{eff} is the effective radius of dendrogram structures and defined earlier. The obtained PCC r -value and p -value of $M - R$ plot are 0.92, and 5.4×10^{-7} , respectively. This indicates the strong positive correlation between mass and radius of dendrogram structures, which is consistent with previous studies (e.g., Kauffmann et al. 2010a,b; Kauffmann & Pillai 2010; Ballesteros-Paredes et al. 2019). In the case of nearby molecular clouds, the $M - R$ power-law index is close to 2 (e.g., Lombardi et al. 2010; Lada & Dame 2020; Cahlon et al. 2023, and references therein). For distant clouds spread over the entire Galaxy this index is found to be >2 (e.g., Miville-Deschênes et al. 2017; Traficante et al. 2018b). However, Ballesteros-Paredes et al. (2019) suggest that the larger power-law index could result from the superposition of line-of-sight dust emission. Additionally, they also pointed out

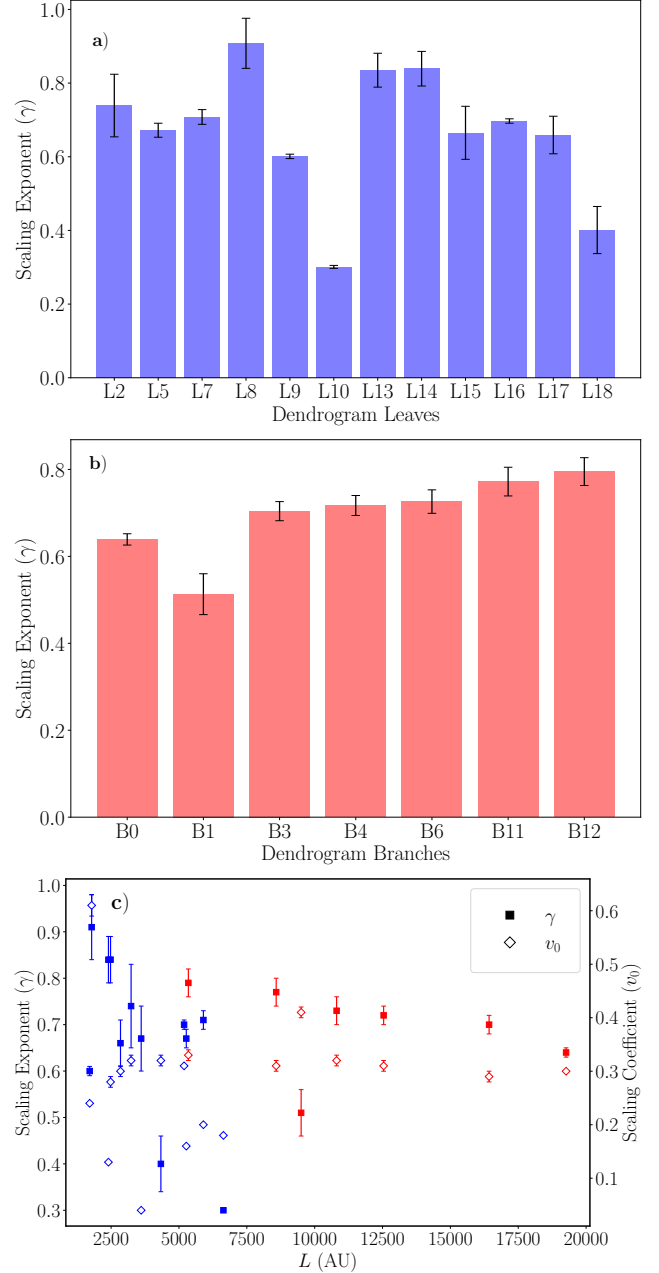


Figure 11. Distribution of scaling exponent (γ) defined in the VSF of second order $S_2(l)^{1/2} = \delta v = v_0 l^\gamma$ for a) dendrogram leaves and b) branches. c) Variation of γ and v_0 with respect to the structure size. Blue and red colors indicate the leaves and branches, respectively. The parameters γ and v_0 are obtained from the power-law best fit for the $S_2(l)^{1/2}$ of each dendrogram structure. The errors denote 1 sigma standard errors on the fitted parameters.

that the $M - R$ relation is dependent on how the cloud structure is defined, e.g., the column density cutoff leads to the power-law index of 2, while the volume density definitions results in the index value of 3 (see also Cahlon et al. 2023).

Earlier, Kauffmann & Pillai (2010) proposed an empirical mass–size threshold for MSF which is based on the clouds with and without MSF. These authors showed that density structures with $m(r) > 870 M_\odot (r/pc)^{1.33}$ are prone to form massive stars. In our analysis, we noticed that only leaf L17 lies within this rela-

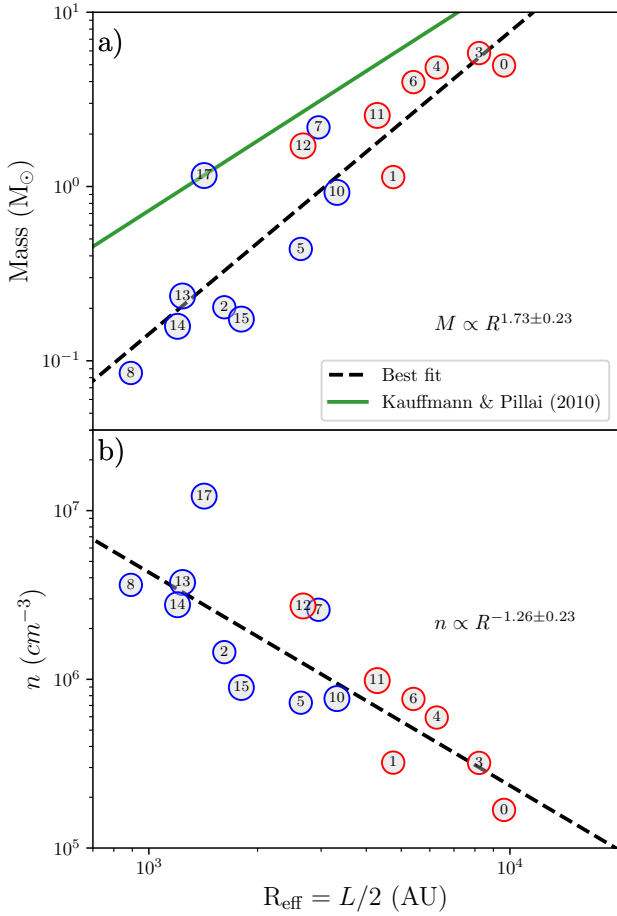


Figure 12. a) Mass–size relation and b) density–size relation of dendrogram structures. Blue (red) circles with labels denote the leaf (branch) structures. A green line indicates the mass–size law of $m(r) > 870 M_{\odot}(r/pc)^{1.33}$ for massive star forming clumps proposed by Kauffmann & Pillai (2010), while dashed line in each panel represents the best fit. The best fit equation is also labeled in each panel.

tion. Infact, leaf L17 was earlier proposed and confirmed as young massive protostar by Dewangan et al. (2015a, 2022b) (see also De Buizer et al. 2022). In a similar way, a plot of mass vs. surface density ($\Sigma = \frac{M}{\pi R_{\text{eff}}^2}$; not shown here) displays a scatter with only leaf L17 satisfying the condition of MSF with $\Sigma > 1 \text{ g cm}^{-2}$ (e.g., Urquhart et al. 2014; Saha et al. 2022).

Figure 12b shows the $n - R$ relation for dendrogram structures. The PCC r -value and p -values are -0.5 , and 0.05 , respectively implying the marginally statistically significant anti-correlation between density and size. The power-law form of density–size relation is observed as $n \propto R_{\text{eff}}^{-1.26 \pm 0.23}$. Here we note a caveat that some of the anti-correlation in the $n - R$ relation is there by construction, given that both the axes depend on the value of R_{eff} (i.e., $L = 2 \times R_{\text{eff}}$ and $n_{\text{H}_2} = \frac{M_s}{(\frac{4}{3}\pi R_{\text{eff}}^3)(2.8 m_{\text{H}})}$; see Section 3.2.2).

3.5 ALMA 865 μm dust continuum cores

In Section 3.1.1, we extracted dendrogram leaf structures from the ALMA H^{13}CO^+ emission and estimated their physical properties, including mass, virial mass, and virial parameter. We noticed that larger values of virial parameters can arise due to the lack of sig-

nificant dust emission within structures where H^{13}CO^+ emission is observed, as shown in Table 1. To address this issue, we identified dust cores (or leaf structures in dust continuum map) using the dendrogram methodology on the ALMA 865 μm continuum map and estimated the aforementioned physical parameters. In order to identify the cores, the parameters “min_value” and “min_delta” were set to be $0.5 \text{ mJy beam}^{-1}$ and $0.2 \text{ mJy beam}^{-1}$, respectively. The parameter “min_npix” was chosen such that the cores contains at least 2 beams of the ALMA 865 μm map (see Section 3.1.1). The analysis resulted in the identification of 14 cores. These dust cores are found to be spatially coexisted with the leaf structures identified in H^{13}CO^+ emission (for comparison see Figures 4 and 13). The size of these dust cores ranges from 1700–6850 AU with mean and median values of 3000 and 2340 AU. The observed mass of dust cores varies from 0.04 to $1.64 M_{\odot}$, and is relatively lower than the mass of H^{13}CO^+ dendrogram leaves (i.e., 0.08 – $2.1 M_{\odot}$; see Table 1). However, the observed mass of these small scale structures is possible because of the missed continuum flux at high resolution ALMA observations, as the interferometric observations are sensitive to strong and compact sources but miss more diffuse and extended emission. Based on this statement the statistics could be slightly biased. Moreover, on scales of ~ 1000 AU, gas-to-dust mass ratios could differ significantly from the canonical value of 100 used for mass calculations on larger scales (Weingartner & Draine 2001). Thus, the low values of mass for these structures (including L17, hosting MYSO) is alone insufficient to discuss their star-forming nature. Also, earlier study by Dewangan et al. (2022b) suggest that the MYSO W42-MME continues to gain mass from its surroundings, which may be true for other dense structures. Figure 13 presents an overlay of the identified core positions by dots on the ALMA 865 μm map displayed with continuum contours. The dot size is proportional to the structure’s footprint area, and the color scale represents the virial parameter information. To estimate the virial mass, we used a mean gas temperature of 54 K, and the mean velocity dispersion for each core was derived using the M_2 map of the ALMA H^{13}CO^+ emission (see Section 3.2). The resulting virial parameter values for the dust cores ranged from ~ 4 to 30, with mean and median values of 15.14 and 14.95, respectively. These values indicate that the dense cores in the W42 region are in overvirial state.

4 DISCUSSION

To examine the physical surroundings of the young massive protostar W42-MME, which is enclosed in a dusty cocoon/envelope (~ 9000 AU) and influenced by the radiative feedback from a nearby massive O5.5-type star (Dewangan et al. 2022b), the investigation of the dense gas kinematics is crucial. Our target site is important since it experiences different environmental conditions compared to young massive protostars that do not belong to the feedback-affected regions by existing nearby massive star (Liu et al. 2022a; Saha et al. 2022). It is worth mentioning that our target site is a part of large filament-hub (extent ~ 1 – 2 pc; see Figure 14 in Dewangan et al. 2022b). These HFSs are widely recognized among the research community as the initial stages of MSF (e.g., Motte et al. 2018; Kumar et al. 2020; Bhadari et al. 2022; Maity et al. 2022; Dewangan et al. 2023a,b, and references therein). Therefore, the study of hierarchical structures of clouds, including clumps and cores, is crucial in understanding how dense cores form within the cloud and the underlying factors involved in this process.

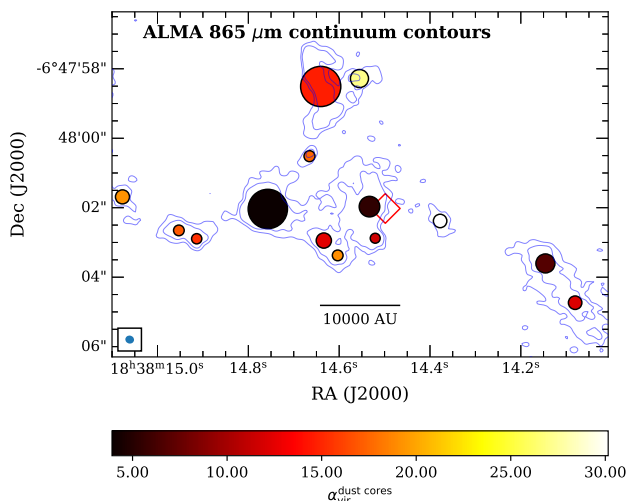


Figure 13. ALMA 865 μm continuum emission contours (levels=[0.4, 1] mJy beam $^{-1}$) overlaid with the positions of dust cores. The size of dots is proportional to the footprint area of dust cores identified in ALMA 865 μm continuum emission map. Color scale signifies the virial parameter of dust cores. The beam size and a scale bar is shown in the image.

4.1 Dynamical state of dense structures

The accurate study of the dynamics of clouds and dense structures in space relies on understanding the nature of gas motion. The leaf structures identified in the dendrogram analysis of ALMA H 13 CO $^+$ data are found to have relatively higher line-of-sight velocity dispersion compared to the branches (see Figure 8). Additionally, all of the identified structures exhibit transonic–supersonic gas motions (i.e., $1 < \mathcal{M} < 5$). These observations are also reflected in the negative trend in $\sigma_{\text{nt}} - L$ plot (see Figure 9). Such a negative trend in the $\sigma_{\text{nt}} - L$ relation is not commonly observed in star-forming clouds. However, some studies show either shallower power-law slope or no correlation as well (Caselli et al. 2002; Traficante et al. 2018b). Widely studied Larson’s first law, on the other hand, suggests a different trend, where large fragments are expected to have higher dispersion compared to smaller ones. The Larson’s relation is found to be consistent at larger scales (> 0.1 pc, e.g., Falgarone et al. 2009; Ballesteros-Paredes et al. 2011), but at a smaller scales the studies are limited (e.g., Li et al. 2020; Liu et al. 2022a; Saha et al. 2022; Li et al. 2023). In this context, our observed $\sigma_{\text{nt}} - L$ relation appear to support the theoretical framework proposed by Ballesteros-Paredes et al. (2018), which emphasizes that the generalized Larson’s relation can have a gravitational origin. Furthermore, for varying column densities, the $\sigma_{\text{nt}} - L$ relation need not necessarily follow Larson’s law. The authors suggest that as the cores collapse, their sizes become smaller, while the column densities and velocity dispersion become larger. This results in an reverse/oblique trend compared to Larson’s relation (see Figure 2 in Ballesteros-Paredes et al. 2018), which can be explained by the consequences of the hierarchical and chaotic collapse scenario. This suggests the emergence of local collapse centers within the entire cloud as it itself undergoes collapse. In such case, the gravitational energy converts to the kinetic energy and develops the virial-like relation (see Figure 2 in Ballesteros-Paredes et al. 2018). We observed the infall gas signature in most of the leaf structures (see Figure 7). Additionally, the identified structures exhibit overvirial ($\alpha_{\text{vir}} > 2$) states, which, as found, are similar to the time evolution of collapsing cores (Ballesteros-Paredes et al. 2018).

These results, present an ambiguous picture if we compare our results with the literature provoking that branches (or clumps) tend to be more turbulent than the leaves (or cores). However, some studies support our observations and advocate the overviriality of cores (Ballesteros-Paredes et al. 2018; Traficante et al. 2018b; Singh et al. 2021; Ramírez-Galeano et al. 2022, and references therein). According to Ballesteros-Paredes et al. (2018), the excess overvirial states is because of the assumption that the gravitational energy is estimated by the energy of isolated homogeneous sphere. They also stress out that such excess disappears when the gravitational energy is correctly estimated from the actual spatial mass distribution. Therefore, the Larson’s $\sigma_{\text{nt}} - L$ relation does not hold when the column densities spanning a large dynamic range are considered. In general, the deviation from the Larson’s scaling can be the signature of gravity-driven chaotic gas motions as predicted by global hierarchical collapse (GHC) model (Ballesteros-Paredes et al. 2011; Vázquez-Semadeni et al. 2019). Our observed scaling relations suggest that the gas motion in the vicinity of W42-MME is transonic-supersonic. The supersonic nature of molecular clouds can arise because of random turbulent motions, gravity-driven chaotic motions, or even ordered motions like localized rotation and outflows, or large-scale directional gas flows (e.g., Li & Burkert 2016; Traficante et al. 2018a,b). In general, the point sources are not promisingly evident in our target region (see Figure 4c), however the dense gas profiles convey the signatures of infall/outflow activities (see Figure 7). These processes can also give rise to high-dispersion values at the smaller scales.

In another approach, the $\delta V_{\text{lsr}} - L$ relation for all the dendrogram structures and $S_2(l)^{1/2}$ for entire region of study, reveal a positive trend and closely follow the generalized Larson’s relation (e.g., Heyer & Brunt 2004) with a nearly constant column density of $\sim 10^{23}$ cm $^{-2}$ and positive scaling exponents of 0.46 ± 0.14 and 0.30 ± 0.01 , respectively. $S_2(l)^{1/2}$, however, tend to be more linear in the regime of < 6000 AU with steeper scaling exponent of 0.68 ± 0.02 . This power-law dependence may indicate general behaviour of velocity field of the gas in the vicinity of W42-MME. It may be possible that the supersonic vortices created by gas motion primarily dominate at the physical scales of leaves (e.g., Dewangan et al. 2019). The power-break in $S_2(l)^{1/2}$ at some length scales has no clear boundary, but our results suggest that the spectral break can occur at around ~ 6000 - 8000 AU scale. This finding requires verification through more studies conducted at the physical scales of cores (i.e., $\lesssim 0.05$ pc). The spatial distance of ~ 6000 AU, interestingly, is closely matched with the maximum structure size of dendrogram leaves (i.e., ~ 6600 AU). The variation in γ defined in the VSF of second order $S_2(l)^{1/2} = \delta v = v_0 l^\gamma$ for dendrogram leaves is found to be larger compared to that of branches (see Figure 11). This suggests that the local gas motions driven by embedded sources and associated activities (i.e., inflow/outflow) primarily contributes in shaping the VSF power-law over time evolution (e.g., Chira et al. 2019, see Figure 1 therein). For larger fragments of clouds (e.g., clumps), the effect seems to be averaged out and hence the structures tend to show a less scatter in the γ .

Here we note that both $S_2(l)^{1/2}$ and δV (indicating the standard deviation of mean velocities within the spatial structures) closely follow the similar statistics and infer the information of gas motion across the sky plane. Hence they appear to show similar positive trends with L . However, σ , which represents the weighted mean of standard deviations of line profiles at each pixel within the structure, provides information about the gas motions along the line-of-sight. At larger spatial scales, all these parameters can be equivalent as the gas kinematic properties will be averaged out, but

at smaller scales where we expect localized gas motion, they may indicate different physical phenomena.

Overall, our observations support theoretical insights from studies that stress the non-universality of Larson’s relations (Ballesteros-Paredes et al. 2018). In contrast to this, several previous studies support that turbulence plays important role at large scales while gravity primarily works at smaller scales. We, however, suggest that the roles of turbulence and gravity cannot be differentiated by non-thermal gas motion alone at the spatial scales of sub-parsec regime, primarily in the environment where the feedback processes are dominant (e.g., Traficante et al. 2018a). Earlier, Goodman et al. (2009) suggested that, apart from the well-cited role of turbulence at large scales, self-gravity plays a significant role in all possible scales of cloud fragments. Similarly, Ballesteros-Paredes et al. (2011) and their subsequent studies (Ballesteros-Paredes et al. 2018, 2019) emphasize the role of turbulence at smaller core scales. These studies suggest that velocity dispersion in molecular clouds do not entirely depend on spatial scales, but also include surface gas densities. Hence, more observational studies of star-forming regions at sub-parsec scales are required to clearly understand the roles of gravity and turbulence (i.e., driving factors of cloud dynamics).

4.2 Star formation Scenario

The multi-wavelength study at larger scale of W42 region by Dewangan et al. (2015b) shows that the massive O5.5 star and W42-MME form at a $\sim 3 \times 3$ pc² junction of several converging filaments (~ 1 – 3 pc). This junction itself is situated at the waist of a bipolar HII region. This picture emphasize the role of filaments in MSF as discussed by Motte et al. (2018) in their evolutionary scheme of MSF. The HFSs are widely popular and thought to provide a suitable environment for the formation of massive stars (e.g., Kumar et al. 2020). However, within a hub one can expect the interplay of different physical processes driven by gravity, turbulence, and magnetic fields. In our site, the young massive protostar W42-MME resides in close proximity to the O5.5 star (Dewangan et al. 2022b). The massive O5.5 star drives enough mechanical energy in the form of its pressure components (i.e., from HII region, radiation, wind, and by self-gravity; see Dewangan et al. 2015b, for detailed calculations) at the vicinity of W42-MME, thus can overall increase the turbulent properties of gas.

A filamentary morphology of coherent velocity structure (61 – 66 km s⁻¹) of size ~ 0.3 pc spanning east-west direction is observed in H¹³CO⁺ data, containing the dendrogram leaves L18, L16, L7, L17 (including L13, L14), L15, and L10 (see Figures 4b and 5b). It is interesting to note that the spatial separation between the leaf pairs of L17–L7 ($\sim 3''.4$) and L17–L15 ($\sim 2''.4$) is more or less similar. Similarly, it is true for leaf pairs of L17–L16 ($\sim 6''.1$) and L17–L10 ($\sim 6''.6$). This may hint at the filament fragmentation by the combined effect of gravity and turbulence (Inutsuka & Miyama 1992; Nakamura et al. 1993; Inutsuka & Miyama 1997). Earlier Dewangan et al. (2022b) pointed out the presence of at least 5 continuum peaks within a dusty envelope (or branch B11 in our analysis) that hosts W42-MME. We note that only one continuum peak (see peak B in Figure 4 in Dewangan et al. 2022b, also see Figure 13) falls within the ALMA beam. The H¹³CO⁺ data however trace a peak (L14) which is not prominent in the continuum image at $865 \mu\text{m}$. It is possible that the W42-MME (L17) compete for material with the nearby sources L13 and L14, which is supported by the potency of MSF in leaf L17 from M – R plot (Figure 12) and infall signature in the H¹²CO⁺ spectral profile. However, the

further high-resolution line data with the dense gas modeling can infer the onset of the competitive accretion process (Bonnell et al. 2001; Bonnell & Bate 2006). The remaining leaves are observed in the feedback-affected zone, which can be seen in the redshifted velocity range of 66 – 72 km s⁻¹ (Figure 4b). Leaves L5 and L2 appear to have potentially accumulated by the outflow emanating from W42-MME (L17).

5 SUMMARY AND CONCLUSION

We carried out an analysis of the dense gas structures in the immediate surroundings of a young massive protostar W42-MME using high-resolution ($0''.31 \times 0''.25$) ALMA dust continuum and line data. A dendrogram analysis is performed in the p - p - v space, allowing us to trace multi-scale structures and their spatio-kinematic properties. We analyzed the fragmentation and dynamic states of dense structures, considering scales as small as ~ 2000 AU. The major results of our study are as follows:

- The dendrogram analysis of the ALMA H¹³CO⁺ (4–3) data resulted in the identification of 19 dense gas structures, out of which 12 are leaves (mean size ~ 3780 AU) and 7 are branches (mean size ~ 11780 AU). The gas motions in these structures are transonic to supersonic ($1 < \mathcal{M} < 5$) and they show overvirial ($\alpha_{\text{vir}} \geq 2$) states. The infall signature is observed in the H¹²CO⁺ (4–3) line profiles of most of the leaves.
- The non-thermal line-width size relation ($\sigma_{\text{nt}} - L$) of dendrogram structures overall shows a weak negative correlation. However, velocity-variation (δV_{lsr}) displays strong positive correlation with the structure size and the relation follows the generalized Larson’s law with steeper exponent of 0.46 ± 0.14 at a constant column density of $\sim 10^{23}$ cm⁻². These results agree with the study of Ballesteros-Paredes et al. (2018) and support the hierarchical and chaotic collapse scenario.
- Velocity structure function analysis of H¹³CO⁺ data reveals the strong power-law dependencies ($\propto L^{0.73 \pm 0.01}$) with $L \leq 6000$ AU. The overall mean scaling exponents of structure function for branch structures is found to be relatively larger compared to that for leaves.
- The mass-size relation of dendrogram structures shows positive trend with a power-law exponent of 1.73 ± 0.23 . The density, however, displays a marginally statistically significant anti-correlation with size. The leaf L17 that hosts W42-MME, meets the mass-size conditions for MSF as discussed by Kauffmann & Pillai (2010); Urquhart et al. (2014).

Overall, the star formation history in the vicinity of W42-MME appears to have been influenced by the effect of scale dependent physical processes, that include the combined role of turbulence and gravity.

6 ACKNOWLEDGMENTS

We thank the anonymous referee for providing the valuable comments that improved the quality of the paper. The research work at Physical Research Laboratory is funded by the Department of Space, Government of India. L.E.P., A.G.P. and I.L.Z. acknowledge the support of the IAP State Program FFUF-2021-0005. This research made use of astrodendro, a Python package to compute dendrograms of Astronomical data (<http://www.dendrograms.org/>). This paper makes use of

the following ALMA data: ADS/JAO.ALMA#2018.1.01318.S and ALMA archive data: ADS/JAO.ALMA#2019.1.00195.L. ALMA is a partnership of ESO (representing its member states), NSF (USA) and NINS (Japan), together with NRC (Canada), MOST and ASIAA (Taiwan), and KASI (Republic of Korea), in cooperation with the Republic of Chile. The Joint ALMA Observatory is operated by ESO, AUI/NRAO and NAOJ. This work made use of Astropy:² a community-developed core Python package and an ecosystem of tools and resources for astronomy (Astropy Collaboration et al. 2013, 2018, 2022).

7 DATA AVAILABILITY

The ALMA data (IDs: #2018.1.01318.S and #2019.1.00195.L) underlying this article are available from the publicly accessible JVO ALMA FITS archive¹. The ESO VLT/NACO data underlying this article are available from the publicly accessible ESO website².

REFERENCES

- Aladro R., Martín-Pintado J., Martín S., Mauersberger R., Bayet E., 2011, *A&A*, **525**, A89
- Anderson L. D., Bania T. M., Jackson J. M., Clemens D. P., Heyer M., Simon R., Shah R. Y., Rathborne J. M., 2009, *ApJS*, **181**, 255
- Askne J., Hoglund B., Hjalmarson A., Irvine W. M., 1984, *A&A*, **130**, 311
- Astropy Collaboration et al., 2013, *A&A*, **558**, A33
- Astropy Collaboration et al., 2018, *AJ*, **156**, 123
- Astropy Collaboration et al., 2022, *apj*, **935**, 167
- Ballesteros-Paredes J., Klessen R. S., Mac Low M. M., Vázquez-Semadeni E., 2007, in Reipurth B., Jewitt D., Keil K., eds, *Protostars and Planets V*. p. 63 ([arXiv:astro-ph/0603357](https://arxiv.org/abs/astro-ph/0603357)), doi:10.48550/arXiv.astro-ph/0603357
- Ballesteros-Paredes J., Hartmann L. W., Vázquez-Semadeni E., Heitsch F., Zamora-Avilés M. A., 2011, *MNRAS*, **411**, 65
- Ballesteros-Paredes J., Vázquez-Semadeni E., Palau A., Klessen R. S., 2018, *MNRAS*, **479**, 2112
- Ballesteros-Paredes J., Román-Zúñiga C., Salomé Q., Zamora-Avilés M., Jiménez-Donaire M. J., 2019, *MNRAS*, **490**, 2648
- Bergin E. A., Tafalla M., 2007, *ARA&A*, **45**, 339
- Bergin E. A., Goldsmith P. F., Snell R. L., Ungerechts H., 1994, *ApJ*, **431**, 674
- Bertoldi F., McKee C. F., 1992, *ApJ*, **395**, 140
- Bhadari N. K., Dewangan L. K., Ojha D. K., Pirogov L. E., Maity A. K., 2022, *ApJ*, **930**, 169
- Blum R. D., Conti P. S., Damineli A., 2000, *AJ*, **119**, 1860
- Bolatto A. D., Leroy A. K., Rosolowsky E., Walter F., Blitz L., 2008, *ApJ*, **686**, 948
- Bonnell I. A., Bate M. R., 2006, *MNRAS*, **370**, 488
- Bonnell I. A., Bate M. R., Clarke C. J., Pringle J. E., 2001, *MNRAS*, **323**, 785
- Bracco A., et al., 2017, *A&A*, **604**, A52
- Cahlon S., Zucker C., Goodman A., Lada C., Alves J., 2023, *arXiv e-prints*, p. [arXiv:2308.14794](https://arxiv.org/abs/2308.14794)
- Carolan P. B., et al., 2009, *MNRAS*, **400**, 78
- Caselli P., Benson P. J., Myers P. C., Tafalla M., 2002, *ApJ*, **572**, 238
- Cen R., 2021, *ApJ*, **906**, L4
- Chira R. A., Ibáñez-Mejía J. C., Mac Low M. M., Henning T., 2019, *A&A*, **630**, A97
- De Buizer J. M., Lim W., Karnath N., Radomski J. T., Bonne L., 2022, *ApJ*, **933**, 60
- Dewangan L. K., Mayya Y. D., Luna A., Ojha D. K., 2015a, *ApJ*, **803**, 100
- Dewangan L. K., Luna A., Ojha D. K., Anandarao B. G., Mallick K. K., Mayya Y. D., 2015b, *ApJ*, **811**, 79
- Dewangan L. K., Pirogov L. E., Ryabukhina O. L., Ojha D. K., Zinchenko I., 2019, *ApJ*, **877**, 1
- Dewangan L. K., Pirogov L. E., Bhadari N. K., Maity A. K., 2022a, *MNRAS*, **516**, 2988
- Dewangan L. K., et al., 2022b, *ApJ*, **925**, 41
- Dewangan L. K., Bhadari N. K., Maity A. K., Pandey R., Sharma S., Baug T., Eswaraiah C., 2023a, *Journal of Astrophysics and Astronomy*, **44**, 23
- Dewangan L. K., Bhadari N. K., Men'shchikov A., Chung E. J., Devaraj R., Lee C. W., Maity A. K., Baug T., 2023b, *ApJ*, **946**, 22
- Falgarone E., Pety J., Hily-Blant P., 2009, *A&A*, **507**, 355
- Fall S. M., Frenk C. S., 1983, *AJ*, **88**, 1626
- Federrath C., Klessen R. S., Iapichino L., Beattie J. R., 2021, *Nature Astronomy*, **5**, 365
- Fukui Y., Habe A., Inoue T., Enokiya R., Tachihara K., 2021a, *PASJ*, **73**, S1
- Fukui Y., Inoue T., Hayakawa T., Torii K., 2021b, *PASJ*, **73**, S405
- Fuller G. A., Myers P. C., 1992, *ApJ*, **384**, 523
- Goodman A. A., Barranco J. A., Wilner D. J., Heyer M. H., 1998, *ApJ*, **504**, 223
- Goodman A. A., Rosolowsky E. W., Borkin M. A., Foster J. B., Halle M., Kauffmann J., Pineda J. E., 2009, *Nature*, **457**, 63
- Gregersen E. M., Evans Neal J. I., Zhou S., Choi M., 1997, *ApJ*, **484**, 256
- Hacar A., Tafalla M., 2011, *A&A*, **533**, A34
- Hacar A., Kainulainen J., Tafalla M., Beuther H., Alves J., 2016, *A&A*, **587**, A97
- Hacar A., Tafalla M., Alves J., 2017, *A&A*, **606**, A123
- Hacar A., Clark S., Heitsch F., Kainulainen J., Panopoulou G., Seifried D., Smith R., 2022, *arXiv e-prints*, p. [arXiv:2203.09562](https://arxiv.org/abs/2203.09562)
- Hennebelle P., Inutsuka S.-i., 2019, *Frontiers in Astronomy and Space Sciences*, **6**, 5
- Heyer M. H., Brunt C. M., 2004, *ApJ*, **615**, L45
- Heyer M., Krawczyk C., Duval J., Jackson J. M., 2009, *ApJ*, **699**, 1092
- Inoue T., Fukui Y., 2013, *ApJ*, **774**, L31
- Inutsuka S.-i., Miyama S. M., 1992, *ApJ*, **388**, 392
- Inutsuka S.-i., Miyama S. M., 1997, *ApJ*, **480**, 681
- Izquierdo A. F., et al., 2021, *MNRAS*, **500**, 5268
- Kauffmann J., Pillai T., 2010, *ApJ*, **723**, L7
- Kauffmann J., Bertoldi F., Bourke T. L., Evans N. J. I., Lee C. W., 2008, *A&A*, **487**, 993
- Kauffmann J., Pillai T., Shetty R., Myers P. C., Goodman A. A., 2010a, *ApJ*, **712**, 1137
- Kauffmann J., Pillai T., Shetty R., Myers P. C., Goodman A. A., 2010b, *ApJ*, **716**, 433
- Kim J.-G., Ostriker E. C., Filippova N., 2021, *ApJ*, **911**, 128
- Krumholz M. R., Federrath C., 2019, *Frontiers in Astronomy and Space Sciences*, **6**, 7
- Krumholz M. R., McKee C. F., 2005, *ApJ*, **630**, 250
- Kumar M. S. N., Palmeirim P., Arzoumanian D., Inutsuka S. I., 2020, *A&A*, **642**, A87
- Lada C. J., Dame T. M., 2020, *ApJ*, **898**, 3
- Larson R. B., 1981, *MNRAS*, **194**, 809
- Li G.-X., Burkert A., 2016, *MNRAS*, **461**, 3027
- Li D., Kauffmann J., Zhang Q., Chen W., 2013, *ApJ*, **768**, L5
- Li S., et al., 2020, *ApJ*, **896**, 110
- Li S., et al., 2022, *ApJ*, **926**, 165
- Li S., et al., 2023, *arXiv e-prints*, p. [arXiv:2304.01718](https://arxiv.org/abs/2304.01718)
- Liu H.-L., et al., 2022a, *MNRAS*, **510**, 5009
- Liu H.-L., et al., 2022b, *MNRAS*, **511**, 4480
- Liu H.-L., et al., 2023, *MNRAS*, **511**, 4480
- Lombardi M., Alves J., Lada C. J., 2010, *A&A*, **519**, L7
- Maity A. K., Dewangan L. K., Sano H., Tachihara K., Fukui Y., Bhadari N. K., 2022, *ApJ*, **934**, 2
- Mardones D., Myers P. C., Tafalla M., Wilner D. J., Bachiller R., Garay G., 1997, *ApJ*, **489**, 719
- McKee C. F., Ostriker E. C., 2007, *ARA&A*, **45**, 565

² <http://www.astropy.org>

¹ <http://jvo.nao.ac.jp/portal/alma/archive.do/>

² https://archive.eso.org/eso/eso_archive_main.html

- Miesch M. S., Bally J., 1994, *ApJ*, 429, 645
- Miville-Deschênes M.-A., Murray N., Lee E. J., 2017, *ApJ*, 834, 57
- Motte F., Bontemps S., Louvet F., 2018, *ARA&A*, 56, 41
- Myers P. C., Goodman A. A., 1988, *ApJ*, 329, 392
- Myers P. C., Dame T. M., Thaddeus P., Cohen R. S., Silverberg R. F., Dwek E., Hauser M. G., 1986, *ApJ*, 301, 398
- Nakamura F., Hanawa T., Nakano T., 1993, *PASJ*, 45, 551
- Padoan P., Pan L., Juvela M., Haugbølle T., Nordlund Å., 2020, *ApJ*, 900, 82
- Pineda J. E., et al., 2015, *Nature*, 518, 213
- Pirogov L. E., 2009, *Astronomy Reports*, 53, 1127
- Quiroza C., Rood R. T., Balse D. S., Bania T. M., 2006, *ApJS*, 165, 338
- Ramírez-Galeano L., Ballesteros-Paredes J., Smith R. J., Camacho V., Zamora-Avilés M., 2022, *MNRAS*, 515, 2822
- Rosolowsky E., Leroy A., 2006, *PASP*, 118, 590
- Rosolowsky E. W., Pineda J. E., Kauffmann J., Goodman A. A., 2008, *ApJ*, 679, 1338
- Saha A., et al., 2022, *MNRAS*, 516, 1983
- Santos J. C., Bronfman L., Mendoza E., Lépine J. R. D., Duronea N. U., Merello M., Finger R., 2022, *ApJ*, 925, 3
- Shetty R., Beaumont C. N., Burton M. G., Kelly B. C., Klessen R. S., 2012, *MNRAS*, 425, 720
- Shirley Y. L., 2015, *PASP*, 127, 299
- Shu F. H., Adams F. C., Lizano S., 1987, *ARA&A*, 25, 23
- Singh A., et al., 2021, *ApJ*, 922, 87
- Solomon P. M., Rivolo A. R., Barrett J., Yahil A., 1987, *ApJ*, 319, 730
- Storm S., et al., 2014, *ApJ*, 794, 165
- Teague R., 2019, *Research Notes of the American Astronomical Society*, 3, 74
- Traficante A., Fuller G. A., Smith R. J., Billot N., Duarte-Cabral A., Peretto N., Molinari S., Pineda J. E., 2018a, *MNRAS*, 473, 4975
- Traficante A., et al., 2018b, *MNRAS*, 477, 2220
- Urquhart J. S., et al., 2014, *MNRAS*, 443, 1555
- Vázquez-Semadeni E., Ostriker E. C., Passot T., Gammie C. F., Stone J. M., 2000, in Mannings V., Boss A. P., Russell S. S., eds, *Protostars and Planets IV*. p. 3 ([arXiv:astro-ph/9903066](https://arxiv.org/abs/astro-ph/9903066)), [doi:10.48550/arXiv.astro-ph/9903066](https://doi.org/10.48550/arXiv.astro-ph/9903066)
- Vázquez-Semadeni E., Palau A., Ballesteros-Paredes J., Gómez G. C., Zamora-Avilés M., 2019, *MNRAS*, 490, 3061
- Vutisalchavakul N., Evans Neal J. I., Heyer M., 2016, *ApJ*, 831, 73
- Weingartner J. C., Draine B. T., 2001, *ApJ*, 548, 296
- Xu F.-W., et al., 2023, *MNRAS*, 520, 3259
- Yuan J., et al., 2017, *ApJS*, 231, 11
- Zhou J.-X., Li G.-X., Chen B.-Q., 2022, *MNRAS*, 513, 638